

---

**Cerium (IV) Oxide Nanoparticles:  
Exploring an alternative to enzymatic  
labelling for Point-of-Care Diagnostics**

---

**Daniel Sarcanean**  
Grau en Nanociència i Nanotecnologia

**Tutor:** Dr. Francesc Torres Canals  
**Institute Supervisors:** Dr. Susana Liébana Girona  
Pr. M<sup>a</sup> de les Neus Sabaté Vizcarra



Instituto de Microelectrónica de Barcelona (IMB-CNM-CSIC)

Facultat de Ciències  
Universitat Autònoma de Barcelona

Bachelor's Thesis  
27 August 2023

# Table of Contents

List of Figures . . . . .	III
Acronyms . . . . .	V
List of Symbols . . . . .	VI
<b>Abstract</b>	1
<b>1 Introduction</b>	2
1.1 Context . . . . .	2
1.2 Objectives . . . . .	6
<b>2 Theoretical framework</b>	7
2.1 Electrochemistry . . . . .	7
2.1.1 Electrochemical cell . . . . .	8
2.1.2 Chronoamperometric detection . . . . .	8
2.2 UV-Vis Spectroscopy . . . . .	9
<b>3 Employed methodology</b>	11
3.1 Instrumentation . . . . .	11
3.2 Chemicals and materials . . . . .	11
3.3 Assay set-up . . . . .	12
3.4 Approaching clinical limits . . . . .	13
3.5 Procedures . . . . .	14
3.5.1 Redox system characterization . . . . .	14
3.5.2 Particle characterization . . . . .	14
3.5.3 Kinetic behavior . . . . .	14
3.5.4 Acquisition of the real limit of detection . . . . .	15
<b>4 Results and discussion</b>	16
4.1 System calibration . . . . .	16
4.2 Characterization of the particles . . . . .	17
4.3 Kinetical response . . . . .	19
4.4 Reaching the LOD . . . . .	20

<b>5 Conclusion</b>	23
5.1 Next steps . . . . .	23
<b>Appendices</b>	25
<b>A Screen-printed electrodes' fabrication</b>	26
<b>B Cyclic voltammetry</b>	28
<b>C Absorbance peak of Potassium Ferrocyanide</b>	29
<b>D Calculations of cerias extensive properties and fitting</b>	30
<b>E Characterization by chronoamperometry</b>	32
<b>Bibliography and references</b>	32

# List of Figures

1.1	((A) Immunoassay steps performed on the nitrocellulose layer located on top of the screen-printed cathode. (B) Overview of the immuno-battery working principle: 1) Open device; 2) Anode and cathode sections are connected by magnetically closing the device; 3) Pins on the anode layer eject the absorbent pad located underneath the screen-printed cathode, and 4) Addition of saline electrolyte connects anode and cathode allowing for power generation and readout. (C) Cross-section of the device showing anode and cathode reactions. . . . .	4
1.2	Suggested alternative to SPEED's first proposal. An unknown concentration of antigen is poured into the test layout (1), if the analyte of interest is bound to our stacked antibodies, then a second complementary antibody conjugates into a sandwich-like system (2). By implementing a mediator; in this case ferro, a redox reaction liberates charge (3) which later can be quantified and translated into a known concentration (4). (Elaborated by the author) . . . . .	5
2.1	Theoretical explanation of the chronoamperometric assay, where an oxidized sample slowly drifts away from the working electrode's surface while the reduced specie tends to adsorbate to it. . . . .	9
2.2	Simplified diagram of a typical spectrophotometer function. (Elaborated by the author)	10
3.1	Simplified diagram of the elements that were utilized. (Elaborated by the author) . .	12
4.1	Spectroscopic (A) and chronoamperometric (B) calibration done with quantified concentrations of ferricyanide, (ferri), ranging from 0 to 2.5 mM. In all cases, n=3 except for the blank which has n=20. . . . .	16
4.2	Kinetic resolution of constant 1-hour incubated 2 mM CeO <sub>2</sub> samples with a span of mediator concentrations with varying particle sizes: (A) in-house 3 nm cerias, (B) commercial 4 nm cerias and (C) in-house 7 nm cerias. Each green dot indicates the Ce <sup>4+</sup> proportion per-2 moles of CeO <sub>2</sub> . . . . .	17
4.3	Simulated relation of different particle sizes attaining to their concentration in volume based on the theoretical instrumental LOD. . . . .	18

4.4	TEM images of non-sonicated ( <b>A</b> ) in-house 3 nm cerias, ( <b>B</b> ) commercial 4 nm cerias, ( <b>C</b> ) 7 nm cerias and sonicated ( <b>D</b> ) 40 nm cerias (batch used to show how the procedure works). . . . .	19
4.5	Spectroscopic measurements of various sonicated particles' samples normalized at 0.5 mM ( <b>A</b> ) in contrast to the same particles normalized at 0.5 mM without sonication ( <b>B</b> ). Incubated and measured <i>in situ</i> until 60 min were reached. . . . .	20
4.6	Graphical representations of the respective calibration curves done with varying concentrations of sonicated ( <b>A</b> ) 3 nm cerias, ( <b>B</b> ) 4 nm cerias and ( <b>C</b> ) 7 nm cerias. In all cases, n=2 incubated for a period of 1 hour. . . . .	21
4.7	Interpolation of the experimental data to the fit, adjusting to the concentration in NP per ml the values of the LODs developed in this last subsection. The red fitting represents an approximated mismatch in between the experimental and theoretical values using both final concentrations' average ( $132.7 \pm 14 \mu\text{M}$ ). . . . .	22
A.1	Diagram of SPE fabrication (elaborated by the author). . . . .	26
B.1	Cyclic voltammetry of a ferro/ferri solution immersed in 0.2 M citric/citrate pH 4 buffer. . . . .	28
C.1	UV/Vis spectra of potassium ferrocyanide with a parabolic peak at 420 nm . . . . .	29
E.1	Raw chronoamperometry data of in-home 3 nm cerias ( <b>A</b> ) and the treated data by means of their integral (charge) ( <b>B</b> ), resembling the same compositional graphs as for kinetic studies. n = 2 with an incubation of 1 h. . . . .	32

# Acronyms

**LOD** Limit-of-detection 1, 2, 4, 6, 13–18, 20–24, I, III, IV

**cerias** Cerium (IV) Oxide Nanoparticles 1, 5, 6, 12–17, 19–24, 28, 30–32, II–IV

**SPEED** Self-Powered Engineered Devices 3, 5, 6, 23, III

**ferro** Potassium hexacyanidoferate(II) 1, 5, 13–15, 17, 19, 28, III, IV

**ferri** Potassium hexacyanidoferate(III) 1, 6, 12–14, 16, 28, III, IV

**TEM** Transmission Electron Microscope 1, 11, 18–21, IV

**SPE** Screen-Printed Electrodes 1, 12, 14, 26, IV

**PCT** Procalcitonin 1

**NAAT** Nucleic Acid Amplification Test 2

**RT-PCR** Reverse Transcription Polymerase Chain Reaction 2

**ELISA** Enzyme-Linked ImmunoSorbent Assay 2

**WHO** World Health Organization 2

**POC** Point Of Care 3, 19, 23

**HRP** Horseradish peroxidase 3–5, 23

**CRP** C-Reactive Protein 3, 4

**HQ** Hydroquinone 4

**BQ** Benzoquinone 4

**LOQ** Limit-of-quanitification 4

**TMAOH** Tetramethylammonium hydroxide 11, 20

**TNF- $\alpha$**  Tumour necrosis factor alpha 13

**LPS** Lipopolysaccharides 13

**XRD** X-ray diffraction 17

**DLS** Dynamic Light Scattering 18

# Abstract

In the context of electrochemical immunodetection for lateral flow diagnostics, this study evaluates the feasibility of utilizing cerium (IV) oxide nanoparticles (cerias) as an alternative to enzymatic labelling, particularly under acidic conditions, provided that they do not need a substrate to work, would get consumed by the test's end and have proved outstanding replicability due to their inorganic nature. The research harnesses manually fabricated screen-printed electrodes' (SPE) environmentally friendly capabilities in concert with a citrate/citric buffer to standardize solutions at pH 4. Ferro/Ferricyanide (ferro/ferri) was used as a mediator, chosen based on its prior proven ability to enhance ceras' absorbance. A comparison of calibration curves was established between conventionally used analysis methods, such as spectroscopy, and chronoamperometry, as adopted in this study. The results indicated a parallel behavior across these diverse physical measurement techniques. Characterization of the particles was achieved via atomic composition through chronoamperometry and UV-spectroscopy, supplemented by size-related studies utilizing transmission electron microscopy (TEM). Kinetic assays further substantiated the utility of these particles for rapid diagnostics, indicating saturation levels within 10 minutes for nearly all the batches measured. Finally, a fit was drawn between the limit-of-detection (LOD) of ceras and contrasted against clinical references, such as gold nanoparticles and procalcitonin (PCT). Experimental findings reveal LODs ranging from  $154.4 \pm 3.9 \mu\text{M}$  to  $111 \pm 13 \mu\text{M}$  for 4 and 7 nm ceras, and adequate subtly to the presented fit, exposing 83.62 nm ceras as the best candidate for proper labeling.

**Keywords:** Cerium (IV) oxide nanoparticles, Lateral flow, Ferrocyanide, Chronoamperometry, Limit of detection.

# Introduction

## 1.1 Context

In the year 1984, a ground-breaking innovation emerged in the field of medical diagnostics, forever changing the landscape of healthcare: the advent of lateral flow tests. These tests made their initial debut in the form of a urine-based pregnancy analysis designed for home use. However, as history often unfolds, the journey of this remarkable invention was not without its challenges. Particularly, being a product primarily targeted towards women, it faced an uphill battle in terms of market acceptance and investor interest in its early stages [1]. One could not imagine that nowadays, with the emerging urge for new diagnostic tools that COVID-19 brought along the pandemic [2, 3], lateral flow devices have gained significant attention as an economical alternative to nucleic acid amplification tests (NAATs) and reverse transcription polymerase chain reaction (RT-PCRs) due to their industrial feasibility and capacity to detect basal infectious rates with little trade-off regarding their LOD. Generally consisting of a three-membrane set-up that favours capillarity among a nitrocellulose strip [4], these devices profit off the chromatographic properties of gun cotton [5] and the conjugation aspects of enzyme-linked immunosorbent assay (ELISA), the latter being discovered in the early 1970s by several research groups at the same time [6, 7] based off the previous radioimmunoassay technique. At present, one can find lateral flow tests in any fashion, from the well-known antigen tests to much more complex self-care systems for multipurpose uses, but the question that follows their potential as a discrimination-free tool towards a more universalized diagnostic remains open. For instance, although the World Health Organization (WHO) encouraged the use of antigen tests since 2020 and still does to this day by the concession of several interims [8, 9], there is evidence that only 0.4% of the total tests were performed in low-income regions by 2022 though they comprise 7.8% of the global population [10]. These adversities fall under the umbrella of the ASSURED (Affordable, Sensitive, Specific, User friendly, Rapid and Robust, Equipment free and Deliverable to end users) criteria set in the 2000s by the WHO, that seeks for more retrospective lateral flow research lines, integrating

these devices as confident point-of-care (POC) diagnostic tools while removing the general uncertainty that many medical guidelines have around them [11]. In the year 2019, these principles were revisited, and two new letters were added, giving the new acronym REASSURED: where the R stands for real-time connectivity and the E for ease of specimen collection and environmental friendliness [12]. Herein, the nature of the tests plays a critical role in their utility and efficacy. The industry largely favours light-dependent assays thanks to their cost of production, colorimetric ones at the forefront, which rely on visual cues to flag the presence of target analytes. Yet, this seemingly convenient approach often grapples with the ambiguity of interpretation. Electrochemical-backed devices, on the other hand, can be seen as a more precise and swifter alternative [1]. They stand apart, not just by providing quantifiable data, thereby reducing the bottleneck of human interpretation, but also by their transformation into single-piece degradable systems. This novelty unveils a double boon: one, enhancing the sensor's analyte detection capabilities, and two, slashing the dependency on specialized laboratory equipment, a sticking point for their low-cost, high-end counterparts. Perhaps one of the most compelling attributes of these electrochemical devices is their capacity to digitize clinical data [13]. This trait propels them far ahead in terms of accessibility and interpretability, as compared to conventional tests. A breakthrough such as this can catalyse the introduction of new POC diagnostic tools, equipping even resource-limited countries to track diseases at the same pace their developed counterparts do.

However, this pursuit of global diagnostic accessibility should not turn a blind eye to the environmental cost of mass production, as we focused on before. With domestic electronics infiltrating pristine regions, pollution has become an undeniable concern. To counteract this, fresh production models that shield environmentally friendly manufacturing to palliate the disadvantages of a "want-it-right-now" economical model have emerged. This research sphere, which focuses on crafting degradable devices and circumvents the collateral damage of swift diagnostics, goes by the name of circular economy [14]. At the Self-Powered Engineered Devices Research Group (SPEED), part of the Microelectronics Institute of Barcelona, IMB-CNM (CSIC), this ethos of sustainable innovation thrives. Here, where the place for this work displayed, the prime objective is to orchestrate specialized sensing tools that marry precision, accessibility, and eco-responsibility.

One of the many examples of SPEED's activity, and which highly influenced the present work by constituting a solid framework, is the creation of a self-powered immunosensor that uses horseradish peroxidase (HRP) for c-reactive protein (CRP) diagnose [15]. This device, named Immuno-battery, is based on the properties of electrochemical immunoassays, comprising both an anode and a cathode to sustain a favorable redox reaction and generate power in the process. It consists of two

layers: a bottom layer with a carbon cathode, nitrocellulose layer, and absorbent pad for immunoassay incubation and solution drainage, and a top layer with a magnesium strip anode connected to a glass-fibre electrolyte support. These layers are assembled using adhesives and a vinyl layer, keeping anode and cathode designed to avoid contact. After completing immunoassay steps, the top layer is added using pins and magnets, and saline electrolyte is introduced for self-powered operation. The device operates by utilizing magnesium oxidation for the anodic reaction and reducing an oxidized redox mediator in the cathode (fig. 1.1), transforming hydroquinone (HQ) to benzoquinone (BQ) thanks to HRP and hydrogen peroxide ( $H_2O_2$ ). The battery's electrode reactions include  $Mg \longrightarrow Mg^{2+} + 2 e^-$  (anode) and  $BQ + 2 e^- + 2 H^+ \longrightarrow HQ$  (cathode), leading to  $BQ + 2 H^+ + Mg \longrightarrow HQ + Mg^{2+}$  overall. The generated oxidized mediator (BQ) mirrors HRP-labelled antibody and captured CRP levels in the nitrocellulose, while device power relates to sample CRP via a non-limiting current anode design. Thanks to its modeling, the immuno-battery achieves a maximum power density of  $571 \text{ W cm}^{-2}$ , higher than previous self-powered immunosensors, and its power peaks occur at operational voltages of 1.5 V, eliminating the need for a charge-pump for low-power electronic modules. Its LOD is determined as  $20 \pm 2 \text{ ng mL}^{-1}$  and the Limit-of-Quantification (LOQ) as 31

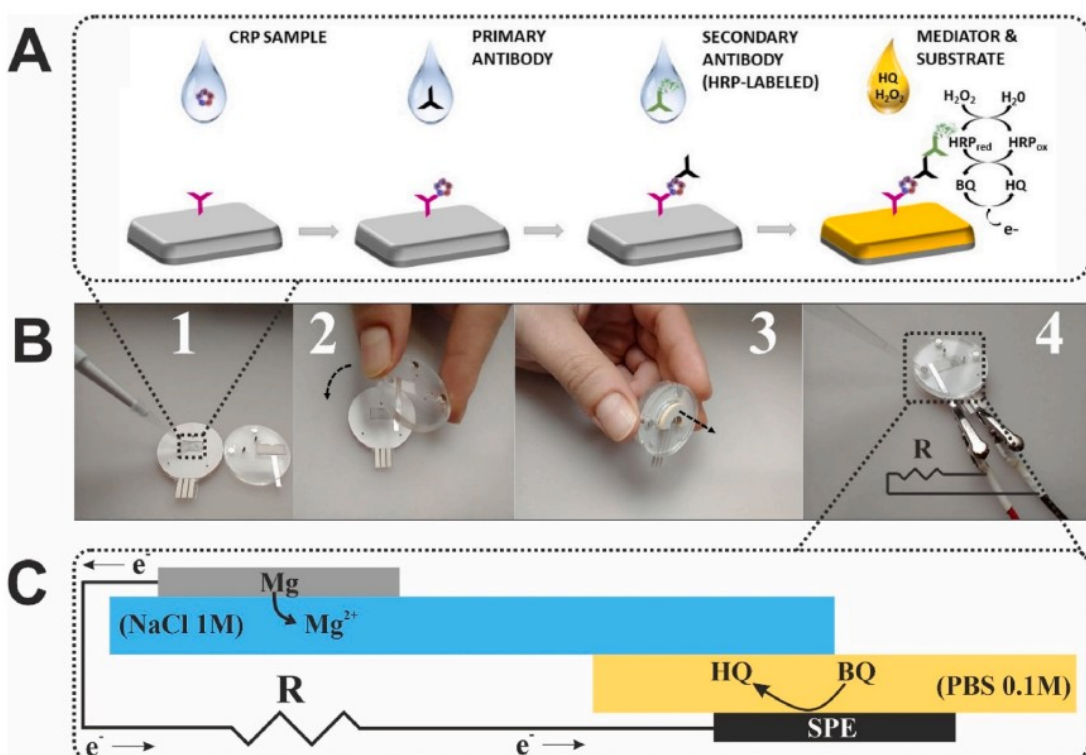


Figure 1.1: **(A)** Immunoassay steps performed on the nitrocellulose layer located on top of the screen-printed cathode. **(B)** Overview of the immuno-battery working principle: 1) Open device; 2) Anode and cathode sections are connected by magnetically closing the device; 3) Pins on the anode layer eject the absorbent pad located underneath the screen-printed cathode, and 4) Addition of saline electrolyte connects anode and cathode allowing for power generation and readout. **(C)** Cross-section of the device showing anode and cathode reactions. (Fig. 2 from Galyamin, D. et al., 2023 [15]).

$\pm 3 \text{ ng mL}^{-1}$  for antibody concentrations. Consequently, the device shows that electrochemical sensors can operate autonomously without sacrificing sensitivity, even letting space for further signal digitization.

Nevertheless, a major distinction concerning standardized methods lies in the selection of an appropriate label. For example, while other lateral flow systems utilize *in situ* conjugation, such as antigen tests, electrochemical analogues require the adaptation of unrestricted systems commonly found in laboratories, and which depend on enzymatic reactions, commonly based on HRP conjugates where the introduction of volatile reactants like hydrogen peroxide is a routine practice. This is precisely the case of SPEED's Immuno-battery. In isolated devices, one must be very cautious about each of the components that perform the detection, not only due to their toxicity and degradable effects, but also contemplating their proper usability. For this purpose, many substitutes have been proposed as adequate replacements for the enzymes' role in conventional lateral flow tests [16]. One of these proposals has been the subject of this study: cerium (IV) oxide nanoparticles (cerias), which have been included as potential substitutes for HRP labeling following Immuno-battery's design (fig. 1.2). Although these particles are much known from their enzymatic-like, antioxidant and renewable capabilities at physiological pH [17], they have shown much more interesting phenomena for immunological detection at acidic conditions [18], where the reaction with the substrate is finite and therefore one can correlate

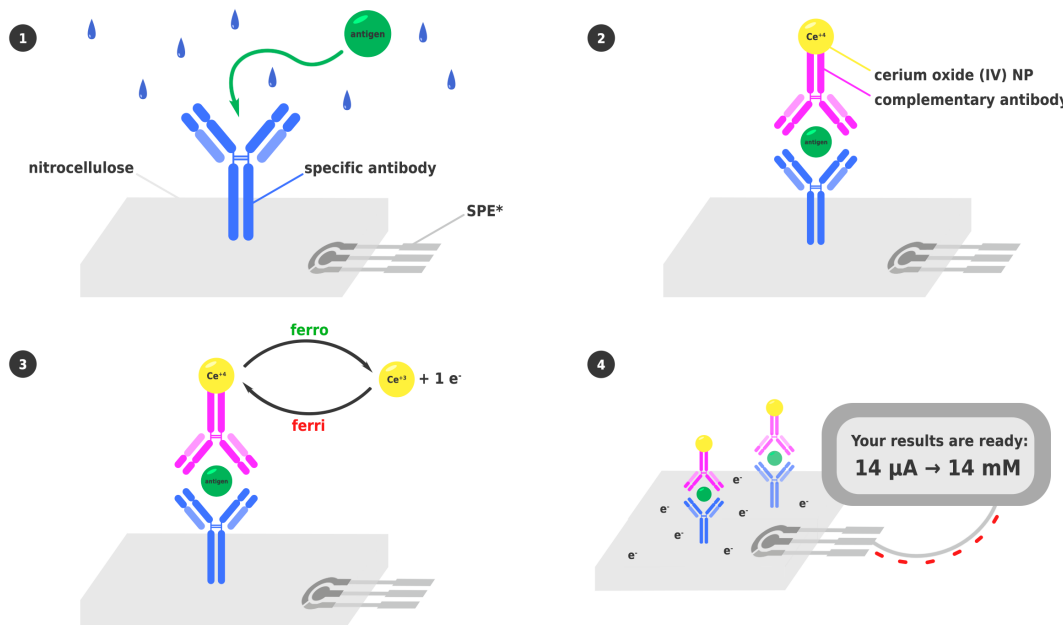


Figure 1.2: Suggested alternative to SPEED's first proposal. An unknown concentration of antigen is poured into the test layout (1), if the analyte of interest is bound to our stacked antibodies, then a second complementary antibody conjugates into a sandwich-like system (2). By implementing a mediator; in this case ferro, a redox reaction liberates charge (3) which later can be quantified and translated into a known concentration (4). (Elaborated by the author)

electrochemical magnitudes directly to the quantity of analyte present in the sample. Since nanoparticles maximize superficial effects, charge exchanges within this dimension are out of the ordinary, although paying with lattice displacements and thus creating intermediary particles that combine both oxidative states:  $\text{Ce}^{4+}$  and  $\text{Ce}^{3+}$  [19], which there is no interest for if the need to abuse their oxidative strength prevails. In fact, cerias' activity can vary regarding on size, pH, temperature, the aggregation state of the particles and interactions with the medium, so validating that these conditions get along with those of the working device is crucial for a proper label selection.

## 1.2 Objectives

The immediate purpose of this work is assessing, experimentally and theoretically, the viability of cerium (IV) oxide nanoparticles as immunoassay labels compared to current cutting edge clinical examples (enzymes and gold nanoparticles). Aiming for future inclusion in a mixed-layout device, which is purely a modification of the cathodic region of the Immuno-battery [15] proposed by SPEED in 2023. To do so, it is needed to determine ferri's limit-of-detection and translate this regression into the same system with present nanoparticles. Achieving this goal includes analyzing how prevalent is  $\text{Ce}^{4+}$  in composition, the spatial arrangement of the particles and their experimental limits of detection for further diagnostic applications, while exploring the profitability of their kinetic properties for electrochemical sensing. Other major aspects involve representing theoretically the ideal particle in order to maximize the discovered LOD, integrating this into a visually simple fit and then correlate with it all the acknowledgments made during the work's course.

# Theoretical framework

## 2.1 Electrochemistry

Any conducting surface immersed in a solution provides a solid phase for electron transfer, for which there is an inherent energy barrier due to the excluding nature of both carriers, electrons and ions. This whole interaction translates into a reduction-oxidation reaction, or redox, and can be written in the form



where O calls for the oxidized form of the analyte, R for the reduced form and  $n$  for the electrons exchanged in the process [20]. This reaction can be either reversible, where both species are always encountered in the medium, or not. The energy involved in the process is given theoretically by the Nernst Potential, which comes simplified for standard conditions as:

$$E = E^0 - \frac{0.0592}{n} \log Q \text{ [V]} \quad (2.2)$$

Here,  $E^0$  is the standard potential of the reaction (referenced normally as the reduction potential) and  $Q$  is the reaction quotient. For liquid reactants, the reaction quotient acknowledges the concentrations and their stoichiometric proportions so the potential involved in the reaction is proportional to the extensive properties of the matter in the solution. Normally, several electrolytes such as NaCl are added to improve ion mobility, if possible. For an even deeper understanding, the optimization of variables like the surface's geometry [21, 22] and the composition of the electrodes [23] are crucial for a well functioning reaction.

### 2.1.1 Electrochemical cell

To conduct an electrochemical study, one requires an electrochemical cell. These usually comprise two or three electrodes, with the working (also known as the indicator) and reference always being necessary. The former serves as the analytical electrode, thereby demanding durability to accommodate high current flows. The latter needs to generate a consistent potential when placed in a solution. To fulfill this requirement, autonomous reference electrodes like hydrogen, Hg/Hg<sub>2</sub>Cl<sub>2</sub> or Ag/AgCl are frequently utilized. In addition to said two electrodes, a counter is usually present to create a bias within the solution the system is immersed. With the advances in nanofabrication and development in newer techniques, electrochemical cells have passed from the common potentiometric membranes to much portable devices, as for examples screen-printed electrodes, due to their less environmental costs and application in biosensing capabilities [24].

### 2.1.2 Chronoamperometric detection

Voltammetric methods comprise of applying a voltage between the working and counter electrodes that involves the reduction or oxidation of one of the species present in the solution. By doing so, and considering the dimensional properties of the electrodes out-scale those of the solution components (so the boundaries are virtually infinite), one can define a transferred one-dimensional mass diffusion equation

$$i_F = \frac{dQ}{dt} = nFA \frac{\partial N}{\partial t} \Big|_{x=0} \quad (2.3)$$

which is related to the charge equation:  $Q = nFNA$  where  $N$  is the amount of Moles either oxidized or reduced in the process,  $F$  is the Faradaic constant equivalent to 96485 C and  $A$  the effective surface area of the electrode. This equation is known as the Faradaic current and can be solved for Fick's laws in a single axis to give Cottrell's equation [25]:

$$i_F(t) = nFAC_i^* \frac{\sqrt[2]{D}}{\sqrt{\pi t}} \quad (2.4)$$

Where  $C_i^*$  is the original concentration of the sample in the solution. A much graphical solution can be seen at fig. 2.1. Note that initially, one finds out there is an infinite current charging the working electrode, due to this reason it is normal to set a relaxation time before starting to measure new data which should not be overextended so still quantifiable current is created.

As seen, chronoamperometric-based diagnostic devices are easy to implement, can serve as keen low-cost sensors for electrosensitive analytes [26, 27], but imply several problems: one that emerges from its time consuming properties and another one due to it being not exclusive to an analyte when tested brute samples, therefore purification steps are commonly mandatory.

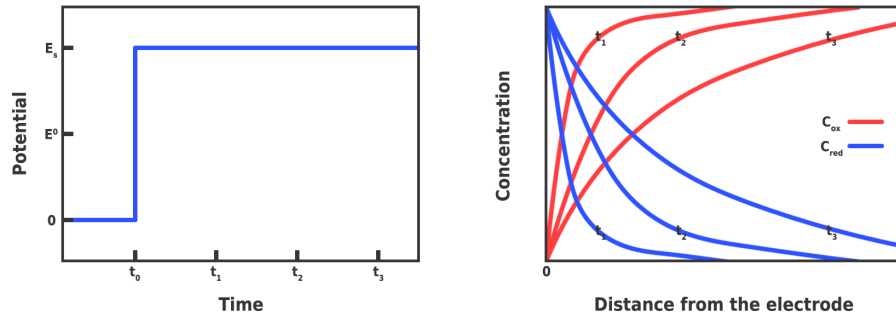


Figure 2.1: Theoretical explanation of the chronoamperometric assay, where an oxidized sample slowly drifts away from the working electrode's surface while the reduced specie tends to adsorbate to it (Adapted by the author from Honeychurch, K.C. [28])

## 2.2 UV-Vis Spectroscopy

Visible and ultraviolet light is also a form of electromagnetic radiation, and so responds to Plank's law of quantised energy,  $E = h\nu$  with  $h$  as Plank's constant and  $\nu$  its respective frequency [29]. Thanks to this characteristic, many atoms and molecules can interact with light absorbing it, and promoting their electrons to upper states (excited states), validating a selection process that has to fulfill quantum mechanics criteria, ergo not all chemical species are undergo this transitions, but only those whose band gaps (differences in energy within basal and excited states) are equal to the incident light's energy. Frequently, one can find less bound electrons to be those that are easily excited with visible light, *e.g.* conjugated systems of aromatic compounds or unstable ionic substances as the energy needed to promote them is arguably small, due to their fairly small energy to transition. Under this scheme, one can use light as an identification utility, to unravel the chemical interactions that appear in certain processes where each compound has a characteristic absorption spectra.

Spectroscopic analysis combine this genuine feature of matter with the much eager discoveries presented by Bouguer P., Lambert J. H. and Beer A. [30–32] by means of the Beer-Lambert law, which relates the absorbed and transmitted light through a medium with the concentration of the absorbent, simplified in the form of

$$A = -\log \frac{I}{I_0} \quad (2.5)$$

where  $A$  is the absorbency and  $I_0$ ;  $I$  are the input and output light intensities. The absorbency can be related to the concentration of the absorbent, or  $c$ , through  $A = \epsilon lc$  where  $l$  is the light's path through the medium and  $\epsilon$  is a property characteristic of the absorbent, which relates to the absorbency coefficient, or  $\alpha$ .

On account of these attributes of light's reactivity, it is possible to develop simplistic but reliable systems, that profit off light emission from a black body emitter, thus a controllable source that relates temperature to light, and complexes based of collimation lens to avoid non-parallel light from arriving to the solution's container or medium where the absorbent is, and thus normalizing light's path for every possible direction (fig. 2.2). The flaws that come attached to this analysis format are that the samples to be tested have to be immersed in transparent vials so light can pass through them (normally in the fashion of cuvettes), and have to be isolated from any other light source. Once performed, a blank with only the background solution or medium is usually mandatory at first, to homogenize the rest of the spectrum taken, and then the measuring can start, either by making sweeps with different wavelengths or only measuring at a constant wavelength.

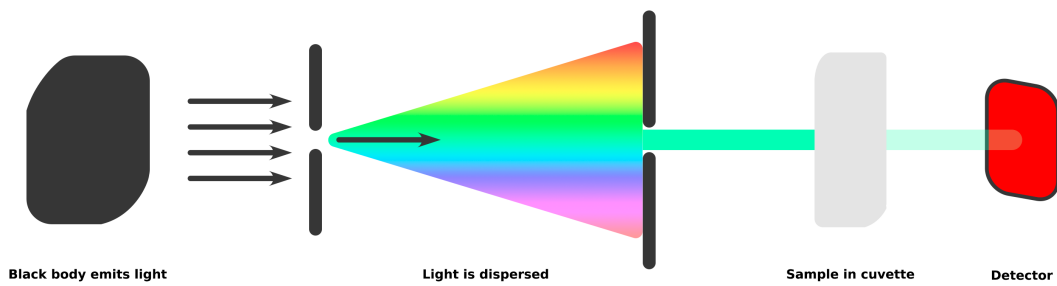


Figure 2.2: Simplified diagram of a typical spectrophotometer function. (Elaborated by the author)

Spectroscopy's utility as a biosensing tool is unparalleled. Its ability to detect and quantify biological molecules, even at extremely low concentrations, makes it indispensable in medical diagnostics, environmental monitoring, and many other areas of bioanalytical and material research.

# Employed methodology

## 3.1 Instrumentation

Spectrophotometric measurements were carried out using a UV-Vis spectrophotometer (Life Science UV/Vis Spectrophotometer, DU 730, Beckman Coulter, US.) through disposable cuvettes (Cat. No. 7591 50, Brand GMBH, DE.). Electrochemical properties were collected using a galvanostat/potentiostat (Dropsens, USTAT400, Metrohm, NL.) tuned with manually made connections. Screen-printed electrodes were hand crafted using a custom-made screen-printing machine (appendix A). Buffer solutions were properly characterized with a pH-meter (pH/Conductometer, 914, Metrohm, NL.). Data treatment was conducted via OriginPro vs. 9.8.0.200 and python programming libraries such as matplotlib vs. 3.6.2. Proposals for the experimental layout were performed with CorelDraw Graphics Suite 2020 vs. 22.1.1523 (Corel Corporation, Ottawa, Canada), prototyped with CO<sub>2</sub> laser cutter Epilog Fusion Edge (EpilogLaser, Golden, CO, USA), cut with a plotter cutter Roland GX-24 CAMM-1 (Roland DG North Europe, DNK) and welded by means of non-flux tin wire. Imaging of the nanoparticles was executed by transmission electron microscopy (TEM) (JEM2010, JEOL Ltd., JP.) over EMR carbon TEM support films (Micro to Nano, 22-IMC040-100, NL.). For in-time sonication a bath sonicator was used (Ultrasons, 3000683, Selecta, ES.).

## 3.2 Chemicals and materials

Different sizes of cerium (IV) oxide nanoparticles were studied: 4 nm 5 % aqueous solution, Ref. PL-CeO-10g, PlasmaChem GmbH, DE.), and 3 nm and 7 nm, stabilized with citrate and tetramethylammonium hydroxide (TMAOH), supplied by the Inorganic Nanoparticles Group led by Prof. Victor Puntes based at the ICN2, Barcelona, ES. [33]. Mediator solutions were prepared in need of the specific species either with potassium hexacyanoferrate (III) (Ref. 60299-100G-F, Sigma-Aldrich, UK.) or potassium hexacyanoferrate (II) trihydrate (Ref. P3289-100G, Sigma-Aldrich, UK.). Buffer solutions were volumetrically prepared with sodium

citrate and citric acid (Ref. S4641-500G and 251275-500G, Sigma-Aldrich, UK.).

Carbon (Ref. C2030519P4, SunChemical, US.), silver (Ref. 2022182, Loctite, US.) and Ag/AgCl (Ref. C2130809D5, SunChemical, US.) pastes were employed in the fabrication of the screen-printed electrodes over a polyethylene terephthalate substrate (PET) (Ref. Elecrom STS, Policrom, IT.). For proper usability, white vinyl was used to delimit the electrodes working area.

### 3.3 Assay set-up

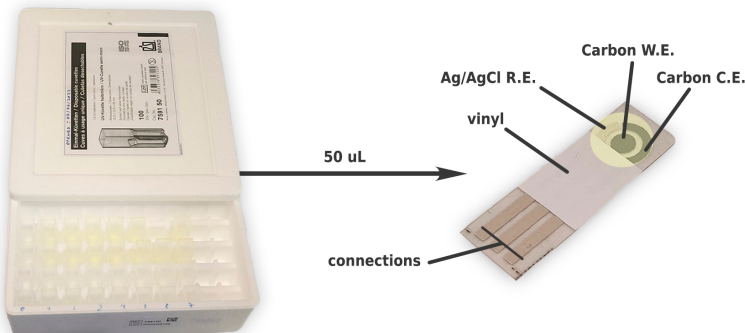
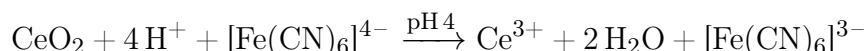


Figure 3.1: Simplified diagram of the elements that were utilized. (Elaborated by the author)

The design shown in fig. 3.1 was employed in the majority of the experimental assays to uniform the data. Cuvettes with known dilutions were incubated and analyzed later in both an amperometric detection mode along the DropSens' utility and a spectrophotometer measuring the concentration at fixed wavelengths favoring the nature of the mediator's redox interaction (-0.2 V). Saline solutions are excluded from the system due to their precipitate-inducing reaction towards cerias functionalized with electrostatic stabilizers, such as is our case. If not used completely, all other assays minimized some of the mentioned components. SPE were designed following the process shown at appendix A. The fundamentals after this set-up were to observe the redox interaction between the cerias and the mediator, described theoretically by this reaction:



The product of said reaction, ferri, can be tracked by its peak in absorbency at 420 nm [18] (seen at appendix C) and contrasted by means of charge generation at

chronoamperometric level. This guarantees that our system of desire has a precise analogue that it is possible to calibrate with and have almost no lose of information in between measuring simultaneously both variables.

The set-up involves a citric-citrate 0.2 M buffer at pH 4. Any other solution done with the reactants involved in the experimental layout are diluted with this buffer to consolidate a final approximated concentration and pH to that of the matrix itself. Mediators are prepared in need of the weight with either ferro or ferri filled up volumetrically with the buffer.

## 3.4 Approaching clinical limits

From the device's theoretical diagram (fig. 1.2), two hypotheses were derived to model antibodies' distribution and therefore cerias' along the nitrocellulose's film. In the first place, considering the paper-strip measured for the prototype had an area of  $0.5 \text{ cm}^2$ , a first spatial approximation of  $5 \cdot 10^{13}$  antibodies was accounted by taking a specific size of 10 nm for each of them, considering full compactability. On the other hand, if the delimitation factor was to be the paper absorption capacity, which ranges from 80 to 100  $\mu\text{g}$  per  $\text{cm}^2$ , and assuming each antibody's molecular weight is of 150 kDa, then the number of antibodies a paper strip would have in a mono-layer array would be of  $1.6 \cdot 10^{14}$  antibodies. These values, assessed as the maximum ones, can be achieved easily with relatively small cerias' concentrations at low sizes (proof by following appendix D), but its desirable tuning them to preferred numbers by increasing the size of the particles and so decreasing the LOD.

To avidly compare cerias capabilities as a labeling material in terms of their LOD, some representative examples were proposed as models. The first being procalcitonin (PCT), as it is an accurate diagnostic tool for tumour necrosis factor (TNF- $\alpha$ ) and lipopolysaccharides (LPS) production, among others, which possesses one of the smallest clinical LODs registered, located at 0.05 ng/ml [34]. This value can be quantified from a total of  $2.316 \cdot 10^9$  particles/ml to  $4.8 \cdot 10^8$  particles/ml (depending on the diagnostic kit used), which is either 4 to 5 magnitudes lower than that registered for the absorption limits commented in the previous section, hence providing an insightful objective to test these particles at: reaching this limit experimentally.

As another contrasting element, gold nanoparticles were chosen, due to their predominance in antigen testing thanks to their plasmonic capabilities. The literature acknowledges a LOD of  $1.16 \cdot 10^{10}$  NP/mm<sup>2</sup> for 3 nm-sized particles, which converted to weight assuming only 7  $\mu\text{L}$  can be absorbed by the paper-strip (due to the dimensional layout the Immuno-Battery has considering nitrocellulose's volume), gives a total of  $8.286 \cdot 10^9$  particles/ml [35].

The key task in this regard is to reach a significant LOD magnitude using the same volume of cerias nanoparticles as the previously suggested concentrations.

## 3.5 Procedures

### 3.5.1 Redox system characterization

The first key for starting to register values is in normalizing the SPE's function range, to do so, a cyclic voltammetry was conducted observing the peaks of reduction and oxidation for ferri/ferro (more in-depth development at appendix B) for pH 4. Moreover, to effectively translate the experimental data from spectroscopic to chronoamperometric values from one to the other a calibration procedure was orchestrated by immersing several solutions of cerias-free dilutions in known concentrations of the mediator's oxidized species (ferri) for later computing a curve for each analytical technique. Herein, a range of dispersed ferri dilutions ranging from 0 to 2.5 mM were introduced in 450  $\mu$ L of a 0.2 M citrate/citric buffer solution and immediately measured through both the spectrophotometer and the potentiostat using previously activated SPE for 5' with a saline solution (NaCl) under a 1.5 V potential. The data treatment conducted for the chronoamperometric proceeded with an integration of the different curves that resulted from the measurement of current along time, thus finding out the charge generated for 60 seconds (a better view of the raw data and treatment can be seen at appendix E given as an example).

### 3.5.2 Particle characterization

For the particle's characterization, solutions of constant 4 mM 250  $\mu$ L cerias (effectively 2 mM in the dissolution), 200  $\mu$ L 0.2 M citrate/citric buffer plus varying concentrations from 0-25 mM mediator (cerias) were incubated for 1 hour long and then registered optically. An analogue was performed chronoamperometrically (appendix E) to show the universality of this application within the two techniques.

### 3.5.3 Kinetic behavior

In the case of kinetic studies, an incubation of known concentrations either of 2 mM (non-sonicated) or 1 mM (sonicated) 250  $\mu$ L solutions were added to 200  $\mu$ L 0.2 M citrate/citric buffer and 50  $\mu$ L of a 50 mM ferro mediator (effectively 5 mM in the final dissolution) was done and measured periodically over an hour taking steps of 10 minutes.

### 3.5.4 Acquisition of the real limit of detection

To conclude, a study over the experimental LOD was performed with dilutions of known cerias' concentrations ranging from 0 to 2.5 mM , 200  $\mu\text{L}$  0.2 M citrate/citric buffer and 50  $\mu\text{L}$  50 mM ferro mediator, which after an hour-long incubation were measured both spectroscopically and electrochemically to enable the building of several LOD predictive curves for sonicated 3 nm, 4 nm and 7 nm particles. A range of equally spaced 0.5 mM solutions of CeO<sub>2</sub> was chosen to then correlate accordingly the content of Ce<sup>4+</sup> present in the samples. The integration curve covers 60 seconds of the current *vs.* time curve.

# Results and discussion

## 4.1 System calibration

The calibration curves derive the instrumental LOD [36], this is, the behavior followed by a steady-state equilibrium within the reactive species. fig. 4.1 shows the spectroscopic and chronoamperometric calibration achieved. For the chronoamperometric measurements, Limit-of-detection was found to be  $7 \pm 3 \mu\text{M}$  obtained from the interpolation of the LOD signal ( $S \text{ LOD}$ ) of  $2.4 \pm 0.4 \mu\text{C}$  (calculated as blank signal +  $1.729^*\text{blank standard deviation}$ , where the multiplying factor follows a t-student for 20 independent samples with a 95% confidence). For the spectroscopic calibration curve, once extrapolated the curve a negative value is obtained, thus the result is inconclusive. Choosing another mediator could solve the problem, due to this system being an internal standard calibration, but the alternatives become less sensitive optically. As briefly commented, the calibration is an idealistic scaffold for measurements involving the reduced species of the mediator and cerias, as it

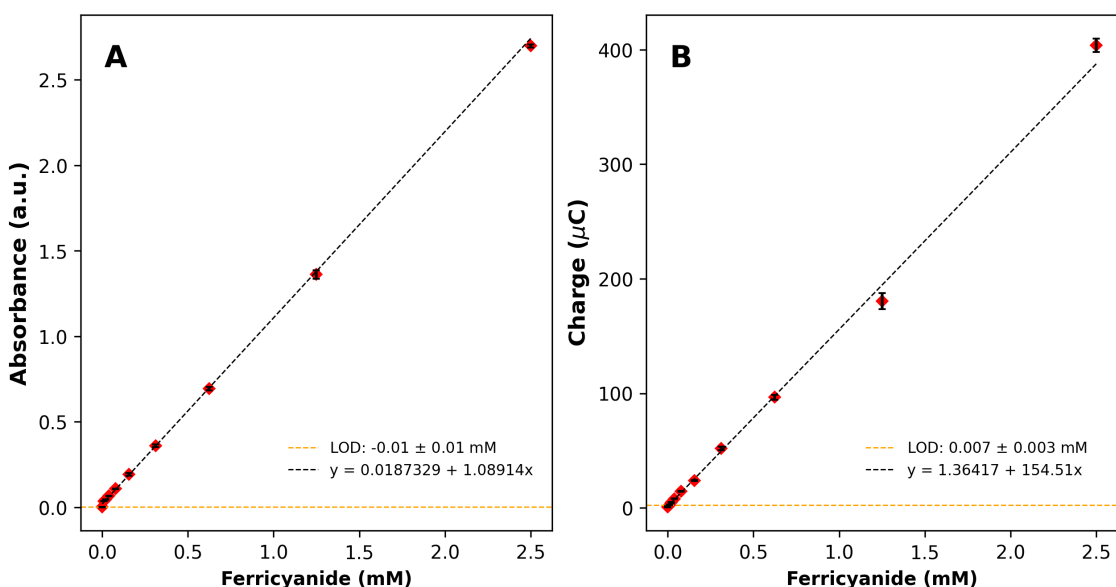


Figure 4.1: Spectroscopic **(A)** and chronoamperometric **(B)** calibration done with quantified concentrations of ferricyanide, (ferri), ranging from 0 to 2.5 mM. In all cases,  $n=3$  except for the blank which has  $n=20$ .

neglects kinetic parameters and diffusion among the dissolution when other molecular structures are present, it is purely the translation of a given signal from one methodology to the other, which can serve as a pathway for future disagreements among them.

## 4.2 Characterization of the particles

$\text{Ce}^{4+}$  composition was found by fitting the particles' oxidative strength through exposition to different concentrations of the reduced specie (ferro) while controlling the exact amount of  $\text{CeO}_2$  involved in the process, results can be viewed at fig. 4.2, where a cross-section was applied assuming that the particles form a plateau once the mediator has been saturated. These curves let us fit the proportional  $\text{Ce}^{4+}$  per mol of  $\text{CeO}_2$  without the need of an x-ray diffraction (XRD) or any other analogue. As seen, an increase in the proportion of  $\text{Ce}^{4+}$  is done in relation to size, the bigger the size the less oxygen vacancies are present, favoring the oxidative strength of cerias. This phenomenon is coherent with the physical behavior of electrons at the nano-scale in cerias, where a 4f molecular orbital delocalization process effects newer oxygen vacancies [37]. For instance, if 3 nm cerias ( $46 \pm 6\% \text{ Ce}^{4+}$ ) are considered in comparison to 7 nm cerias (with  $59 \pm 2\% \text{ Ce}^{4+}$ ) a jump from  $1.539 \cdot 10^{15}$  to  $1.572 \cdot 10^{14}$  NP/ml (appendix D) is perceived, introducing an order of magnitude just by switching in 4 nm the particles' size without losing any signal in detection, matching with the literature for increasing size cerias layouts [38]. Moving forward, this size-dependent property can be used to design a fit that correlates a clue to outperform the theoretical LOD by improving the fabrication of bigger size nanoparticles (fig. 4.3). To do so, an extrapolation of a generic  $\text{Ce}^{4+}/\text{CeO}_2$  ratio regression is made with 3 data sets of different particle sizes (the ones presented at fig. 4.2), and embedded into the following formula:

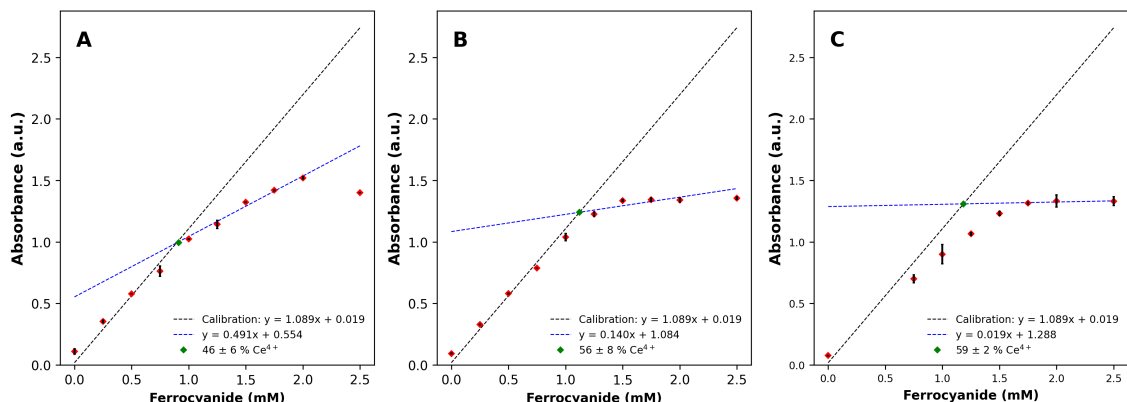


Figure 4.2: Kinetic resolution of constant 1-hour incubated 2 mM  $\text{CeO}_2$  samples with a span of mediator concentrations with varying particle sizes: **(A)** in-house 3 nm cerias, **(B)** commercial 4 nm cerias and **(C)** in-house 7 nm cerias. Each green dot indicates the  $\text{Ce}^{4+}$  proportion per-2 moles of  $\text{CeO}_2$ .

$$\text{NP concentration} = \text{regression} \cdot \frac{1}{\text{particle volume}} \cdot \frac{1}{\text{density}} \cdot \text{mol. weight} \cdot \text{LOD} \quad (4.1)$$

Where each characteristic value is presented at appendix D, and the included LOD comes from to the first calibration subsection. The regression that is achieved translates into a straight fit ( $y = 2.6522 \cdot r + 47.33$ ) which declares a second relation to  $r$ , and hence complicates the fitting's resolution. Nonetheless, if considered that the ratio is constant, it is possible to simply extract  $r$  for said value and then recalculate it using Bernoulli's method (the process is developed in-depth at appendix D). The output is the size for each of the clinical limits that were defined in previous sections, resulting graph can be observed at fig. 4.3.

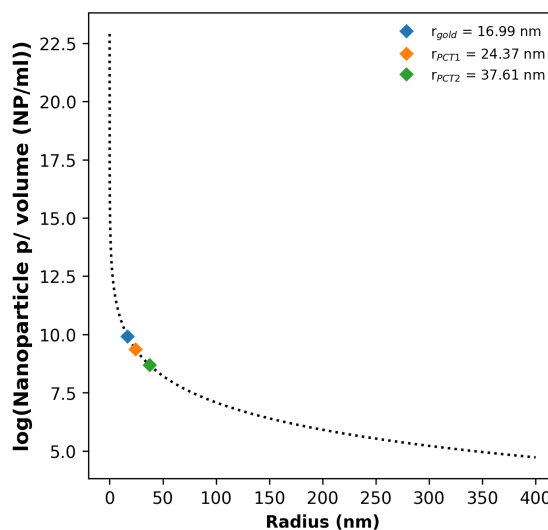


Figure 4.3: Simulated relation of different particle sizes attaining to their concentration in volume based on the theoretical instrumental LOD.

The particles' sizes were obtained by dynamic light scattering (DLS) prior to their acquisition. To ensure the dimensional properties of the particles and see their spatial arrangement, which can later be an important point of study regarding their electrochemical behaviour, TEM images of each are contributed (fig. 4.4). Herein, it is observed that the theoretical oxide sizes do not match with those tagged within the particles, although the measurement is conclusive. This can be due to the nature of each technique, where for the first one a solvated radius is calculated due to Brownian motion in a suspension, and in the second one it is seen that the naked particles are interacting with the solution [39]. Although introduced here as individual particles, most probably what is discerned within DLS is the agglomerated and real radius, whereas in an ambient such as the one it is imposed to the solution in a TEM, generally by applying vacuum, ultra-cold temperatures, and beaming the sample with an electron ray, the particles tend to allocate in infrequent arrangements

and citrate possibly migrates from the particles' surface, giving such characteristic images. However, the sonication procedure to de-agglomerate the particles is verified thanks to TEM images, and can be seen properly at fig. 4.4, where an array of distant particles is observed.

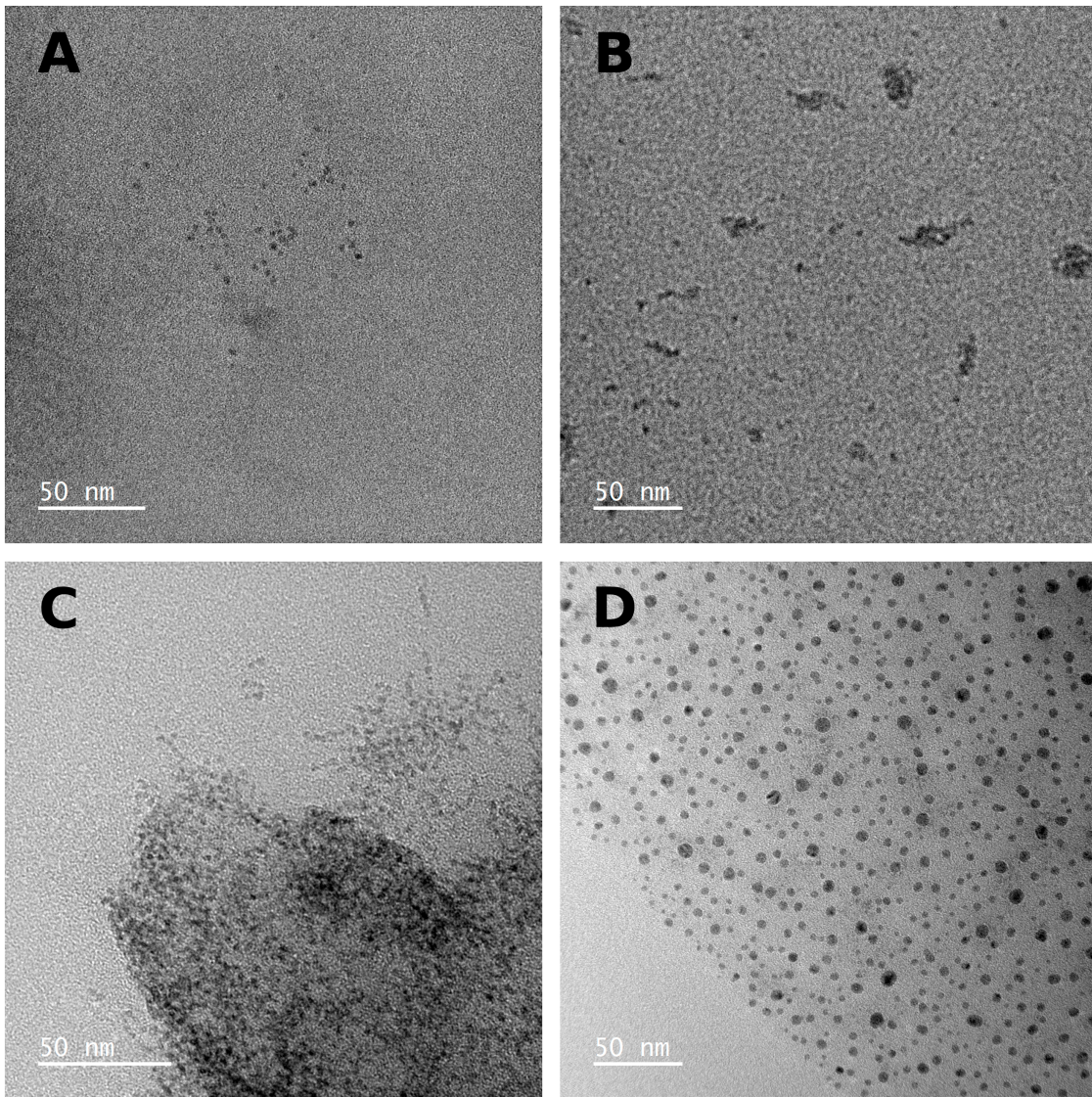


Figure 4.4: TEM images of non-sonicated **(A)** in-house 3 nm cerias, **(B)** commercial 4 nm cerias, **(C)** 7 nm cerias and sonicated **(D)** 40 nm cerias (batch used to show how the procedure works).

### 4.3 Kinetical response

One major issue of electrochemical methods, as mentioned earlier, is their enclosed times of assay. This problem is in contrast with POC devices, as less time-consuming tools are mandatory for better user-friendly diagnostics. Hence, there was a need to also see the applicability of cerias in terms of the time these consume to interact with the mediator, i.e., ferro. By studying the kinetics of cerias not only it is possible to elucidate the time they last to consume all the ferro present in the

solution, but also the interactions they develop depending on which background they come from. To do so, a comparison between non sonicated and sonicated, thus agglomerated and not, can be identified at fig. 4.5. Herein it is possible to see that non-sonicated samples are ‘passivated’ in some way, as sonication ‘activates’ their respective kinetics. This can be taken as an indicative of agglomeration (although as commented before the TEM images are not terminally conclusive due to the experimental nature of the analysis). However, there is not a close relation to particle-size, but on the synthesis’ conditions. Commercial cerias (4 nm) do not differ much in both behaviors, and this can be explained based on their synthesis: as they present *a priori* no superficial stabilizers and are probably curated with hydrogen peroxide to ensure proper activation as an oxidizing factor, ergo saturating the population of Ce<sup>4+</sup> species at the surface. In the other hand, the rest of the particles are stabilized with citrate and dissolved in TMAOH, the first being an electrostatic stabilizer and the second an agglomerate-preventer, therefore it is possible that these two interact if not sonicated to equilibrate the particles’ need to relax their superficial tensions. It is suggested that the problem resides on their aging, although these have shown to be stable, as many favorable thermodynamic processes could have inflicted in their arrangement.

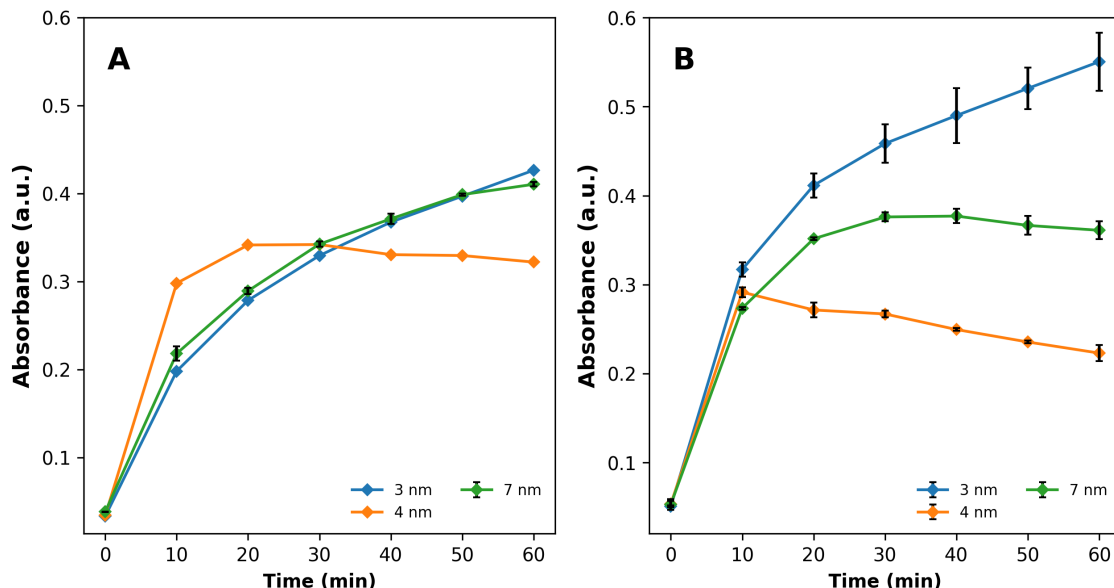


Figure 4.5: Spectroscopic measurements of various sonicated particles’ samples normalized at 0.5 mM (A) in contrast to the same particles normalized at 0.5 mM without sonication (B). Incubated and measured *in situ* until 60 min were reached.

## 4.4 Reaching the LOD

Within the last part of this work’s experimental the goal was to reach out the respective LODs for the particles to observe the differences within the ideal fit introduced in the calibration. Presented in fig. 4.6, an ambiguous determination

of the LOD for each size can be observed but considering the calculated relations (seen more in-depth in appendix D) there is still an improvement in reducing the ultimate particle number in a solution without sacrificing the resulting signal. In addition to this, the use of less time to integrate the curves did improve a little bit the technique's sensitivity, although not enough to be considered as a game-changer due to maintaining the ratios in between the measured samples, hence preserving the integral at 60 s for later usage.

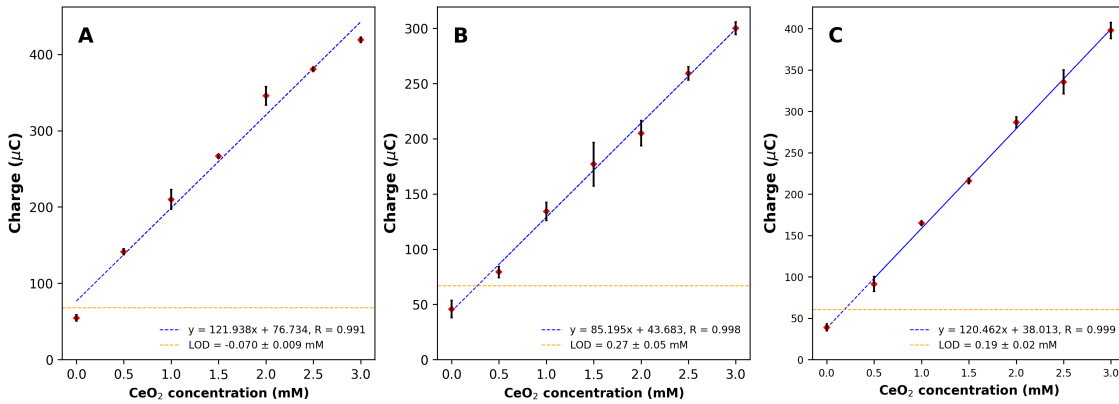


Figure 4.6: Graphical representations of the respective calibration curves done with varying concentrations of sonicated **(A)** 3 nm cerias, **(B)** 4 nm cerias and **(C)** 7 nm cerias. In all cases,  $n=2$  incubated for a period of 1 hour.

Giving a deeper insight to fig. 4.6, the LODs presented are the concentration of  $\text{CeO}_2$  needed for such signals without including the ratio of  $\text{Ce}^{4+}$  each particle has. By adding this percentage, unraveled at the characterization section, it is possible to round up to values of  $154 \pm 4 \mu\text{M}$  for 4 nm cerias and  $111 \pm 13 \mu\text{M}$  for 7 nm cerias. The values for 3 nm samples cannot be employed due to the experimental layout reaching apparently the minimal possible values. Although distant from the  $7 \pm 3 \mu\text{M}$  discovered through the calibration curve, these values can be included in the fit simulated sections before to conceal how far the data is from the theoretical point, and to suggest if it is achievable to some extent to keep increasing the particles' diameter in pro of seeing an effect in the pure LOD.

If this data is introduced into the calibrated fit, it is possible to see a newer curve which reflects the experimental limits for cerias, where an ideal radius can be matched using the data proportioned by the smallest theoretical limit, which is  $4.8 \cdot 10^8 \text{ NP/ml}$ . As seen in fig. 4.7 the data results in particles with diameters exceeding 100 nm, which would categorize them as out of the nanoscale (as per definition, any material is only considered 'nano' if any dimension has less than 100 nm of length). Nevertheless, it is worth proving if their 'nano-properties' are extinguished at such limits, as by the look of their TEM images, superficial crystallization is not isotropic, and hence particles of 83.62 nm still can have nanometric scale dimensions. It must be commented the still varying capabilities of different

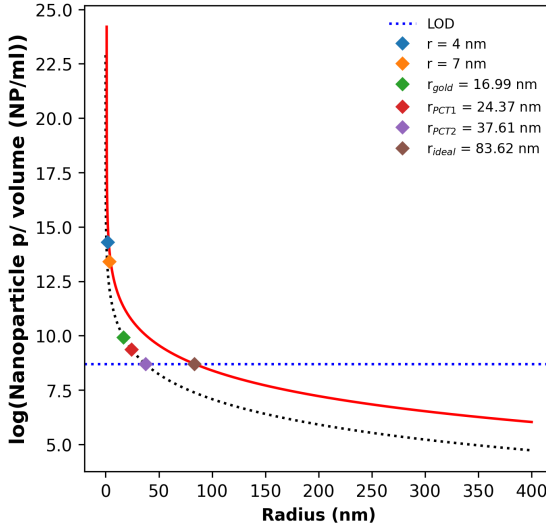


Figure 4.7: Interpolation of the experimental data to the fit, adjusting to the concentration in NP per ml the values of the LODs developed in this last subsection. The red fitting represents an approximated mismatch in between the experimental and theoretical values using both final concentrations' average ( $132.7 \pm 14 \mu\text{M}$ ).

cerias sizes. Each of these sizes cover a spectrum of  $10^3$  units, as an example it is possible to quantify that for 10 mM of a pure 3 nm cerias solution there would be a range from  $1.6 \cdot 10^{16}$  to  $1.6 \cdot 10^{14}$  particles before losing significant action. In the case of bigger cerias the range shortens up, which can be thought logically by looking at the graph. Indeed, there are several clinical ranges that can profit off these intervals, like C-reactive protein [40]. For the interest of the group's research, the question opens into finding the compromise between small enough particles to be convenient for antibody detection and big enough to present a high  $\text{Ce}^{4+}/\text{CeO}_2$  ratio. Moreover, the liability of these particles lies into the replicable samples it gives, and how easy is to functionalize them in case an improvement in their reactivity is needed. There is special attention from the scientific community to the many amplification-like functionalities that have been performed into the conjugation with antibodies for cerias [41, 42], multiplying their response without sacrificing the positive points of using nanoparticles for electrochemical and spectroscopic diagnostics.

# Conclusion

Cerium (IV) oxide nanoparticles, whether citrate-functionalized or not, have exhibited properties comparable to those experimentally observed in HRP [15], achieving an impressive  $50 \mu\text{A}$  with a  $10 \mu\text{M}$  particle solution per  $50 \mu\text{L}$  drop. This contextually high electrochemical efficiency, combined with the ease of treatment, batch homogeneity and handling of nanostructured oxides, positions cerias as promising alternatives for future enzyme-like labeling [43].

The present work reveals that by scaling up their size, these particles can secure a fully saturated surface of  $\text{Ce}^{4+}$  species, thereby maximizing their electrochemical capabilities. We established a spectrum of detection limits, as per the experimental section's criteria, ranging from  $1.6 \cdot 10^{14} \text{ NP/ml}$  for 3 nm cerias to  $2.5 \cdot 10^{13}$  for 7 nm cerias. It was found that to achieve similar LODs to 3 nm gold nanoparticles,  $4.8 \text{ NP/ml}$ , cerias have to be synthesized with a 83.62 nm radius, which can overthrow their latter purpose due to impeding the potential use of their nanometric properties.

Our structural analyses highlighted their stability and facile homogenization procedures, substantiating their role as reliable labels. Indeed, the effortless technique presented by Galyamin, D. and used along this work to verify if  $\text{Ce}^{4+}$  concentration was coherent with the particle size, showed a much easier approach to chemical analysis than other more rigorous techniques, demonstrating that not only the final devices can be optimized for resource-less conditions but also part of the synthesis and laboratory analysis, especially considering that seed-growth methods are achievable with little materials. Additionally, the suitable kinetic ranges suggest a potential fit for POC diagnostics, comparable to familiar antigen tests used during the pandemic.

## 5.1 Next steps

However, while the study met most of its anticipated objectives, some gaps warrant further exploration. Specifically, understanding how conjugation influences reactivity and diffusion within the SPEED group's proposed setup remains a critical next

step. The literature provides valuable insights into these processes [44], particularly for *in vivo* assays, where cerias demonstrate potential for tumor suppression. Another major aspect to take into account, and one that can favor the critical size achieved within the covered results, is that the quantum nature of cerias oxygen vacancy generation goes in contrast to conjugation chemistry, which localizes the electrons implied into the reaction and hence can lower down the required radius. This assumption is important not only due to the reasons mentioned, but also keeping in mind that the smaller the cerias, the bigger the signal's amplification, which would result in a minor LOD. If necessary, future work should focus on developing a representative conjugation complex with a standard antibody or protein and evaluating its physical properties in a drop-like environment or over nitrocellulose.

Additionally, the implications of organic deposition from such devices when cerias are deployed need further investigation. Some studies report positive biocompatibility [45] across a variety of species, while others document unexpected toxicity patterns, predominantly in plants [46]. This calls for an initial field study to understand potential ecosystem impacts before commercializing any diagnostic tool which incorporates cerias. As previously mentioned, the goal of these particles is being part of cost-effective diagnostic devices. Therefore, any major negative consequences, especially when introducing these tools in developing countries, require proper monitoring due to given potential devastating impacts on soil and agriculture.

In conclusion, further studies should prioritize the conjugation of cerias and report the same analytical methods performed here, as well as integrating pH changes or any other substantial conditions for much more unstable or tissue-based analytes. Another big aspect to optimize is the implementation of saline solutions once the system is complexed, for better amperometric detection, seeing if in that medium cerias are still operable or not. Finally, the issue would be integrating the solution and preparing a simplified model for an immunodetector powered with cerias oxidation, looking for a user-friendly type of diagnostic with every aspect being sustainable with the environment.

# Appendices

## Screen-printed electrodes' fabrication

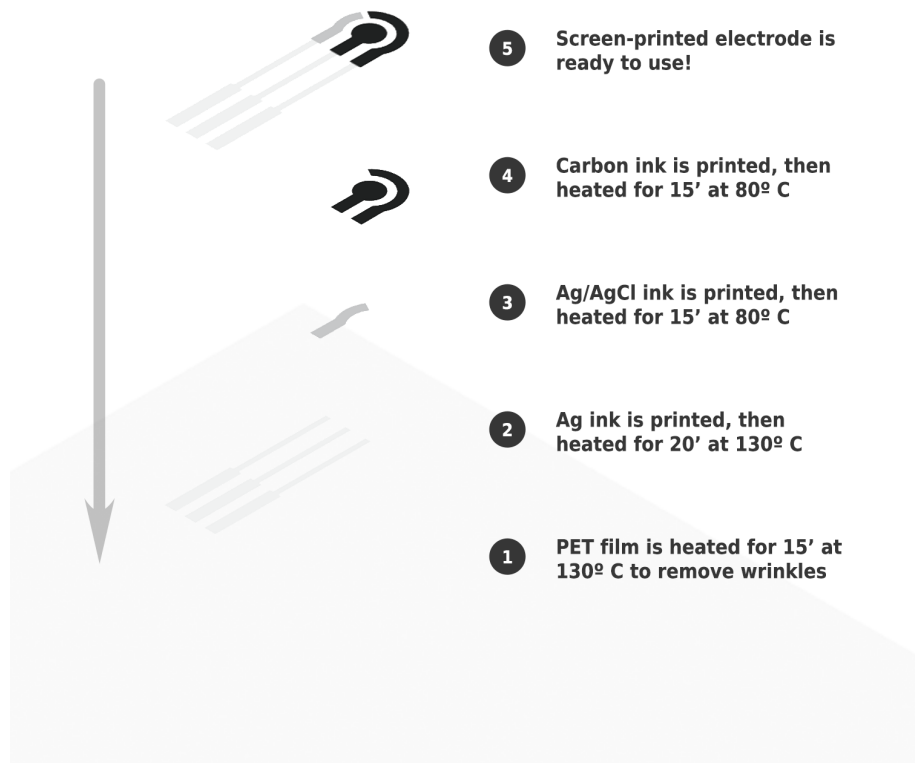


Figure A.1: Diagram of SPE fabrication (elaborated by the author).

*Alternative description:* The three-electrode system used comprises working electrode (WE), counter electrode (CE) and reference electrode (RE). Fabrication of the electrodes was carried out by screen-printing using PET substrate (Ref. Elecrom STS, Policrom, Italy). Firstly, a PET substrate is pre-treated at 130°C for 15' to uniformize the surface. Secondly, silver ink tracks (Ref. SCAG-005, Mateprincs, Spain) are printed and consequently cured at 80°C for 15'. Silver/silver chrolide ink (Ref. C2130905D3, Gwent Group Ltd., UK) is printed as the reference electrode,

curing as well at 80°C for 15'. Finally, carbon ink (Ref. C2030519P4, Gwent Group Ltd., UK) is used to print the working electrode, then cured at 80°C for 15'. Prior to use, a vinyl layer was fixed on top of the silver tracks to isolate them from the liquid and limit the working area where the solution is added. Activation of the electrodes was carried out by adding a 50 µL drop of 100 mmol L<sup>-1</sup> of NaCl and applying a potential of 1.5 V for 5 min. This activation step is crucial to eliminate residues from printing process by oxidizing them before testing.

## Cyclic voltammetry

Cyclic voltammetry was performed in a potential interval from -0.6 V to 0.6 V using exclusively a 50  $\mu$ L 10 mM ferri/ferro solution over the three-electrode system explained in the fabrication appendix. Both peaks are appreciated (reduction and oxidation). Appointing of the reduction's peak voltage is mandatory, as it is required to use voltages lower than this to activate the reduction of ferro to ferri ( $\text{Fe}^{2+} \longrightarrow \text{Fe}^{3+}$ ) and oxidation of cerias ( $\text{Ce}^{4+} \longrightarrow \text{Ce}^{3+}$ ). This voltage is located at 0.08 V for pH 4. In order to achieve a mass-transfer limited current and higher response a potential of -0.2 V is applied in the chronoamperometric studies.

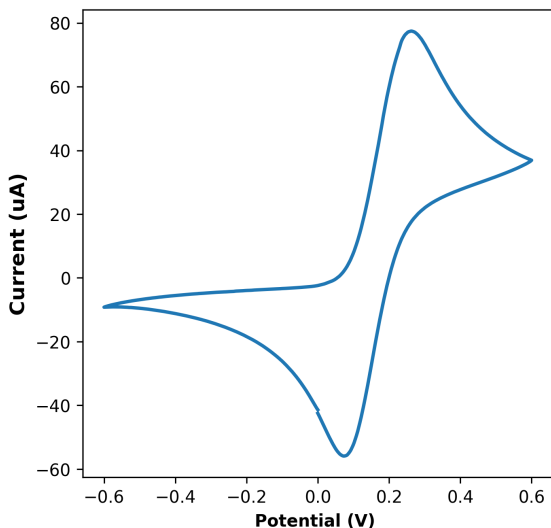


Figure B.1: Cyclic voltammetry of a ferro/ferri solution immersed in 0.2 M citric/citrate pH 4 buffer.

## Absorbance peak of Potassium Ferrocyanide

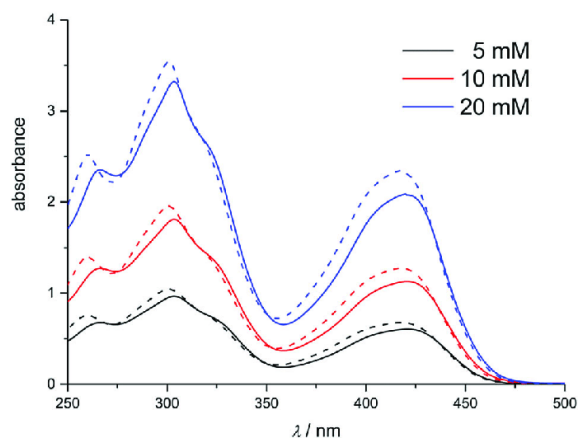


Figure C.1: UV/Vis spectra of potassium ferrocyanide with a parabolic peak at 420 nm (Fig. 2, [47])

# Calculations of cerias extensive properties and fitting

In order to obtain the chemical properties of the particles by hand, these calculations were derived, using cerias characteristic properties: a density of 7220 kg/m<sup>3</sup> and a molecular weight of 172.12 g/mol. At first, to calculate the molarity for each particle size, the following equation was used:

$$[\text{M}] = \text{Particles} \frac{\text{NP}}{\text{mL}} \cdot 1000 \frac{\text{mL}}{\text{L}} \cdot (4/3) \cdot \pi \cdot (r)^3 \frac{\text{m}^3}{\text{NP}} \cdot 7220 \frac{\text{kg}}{\text{m}^3} \cdot \frac{1}{172.12 \cdot 10^{-3}} \frac{\text{mol}}{\text{kg}} \quad (\text{D.1})$$

Then, their concentration in particles (NP/ml):

$$[\text{Particles}] = \frac{1}{7220 \cdot 10^3} \frac{\text{m}^3}{\text{g}} \cdot \frac{1}{(4/3) \cdot \pi \cdot (r)^3} \frac{\text{NP}}{\text{m}^3} \cdot [\text{Molarity}] \quad (\text{D.2})$$

Each of these calculations are independent and can be referred one to the other. In addition, theoretical calculations were proposed for completely covered with Ce<sup>4+</sup> nanoparticles:

$$\text{Ce}^{4+} = 7220 \frac{\text{kg}}{\text{m}^3} \cdot (4/3) \cdot \pi \cdot (r)^3 \frac{\text{m}^3}{\text{NP}} \cdot \frac{1}{172.12 \cdot 10^{-3}} \frac{\text{mol}}{\text{kg}} \cdot 6.022 \cdot 10^{23} \frac{\text{CeO}_2}{\text{mol}} \quad (\text{D.3})$$

The fitting calculation includes a first step of a constant recovery, as:

$$r^3 \cdot \frac{2.6522 \cdot r + 47.33}{100} = \left[ \frac{1}{4/3\pi(1 \cdot 10^{-9})^3} \cdot \frac{1}{\text{density}} \cdot \text{weight} \cdot \text{LOD} \cdot \frac{1}{\text{conc.}} \right]^3 \quad (\text{D.4})$$

Herein, Ruffini's theorem is applied to unravel a theoretical radius:

$$r^3 \cdot \frac{2.6522 \cdot r + 47.33}{100} = \text{ct.} \quad (\text{D.5})$$

Giving either a real radius, or a negative one, which can be neglected. All the data is included later on into the fit, and results can be seen at any graph following fitting's pattern.

# Characterization by chronoamperometry

The Ce<sup>4+</sup> ratio can also be found following electrochemical criteria, thanks to the redox nature of the reaction. An example of this can be viewed in at the following graph, were samples of 3 nm cerias suffered a fixed potential reaction in an amperometric basis. Raw data is attached to show how the data treatment translated into the results.

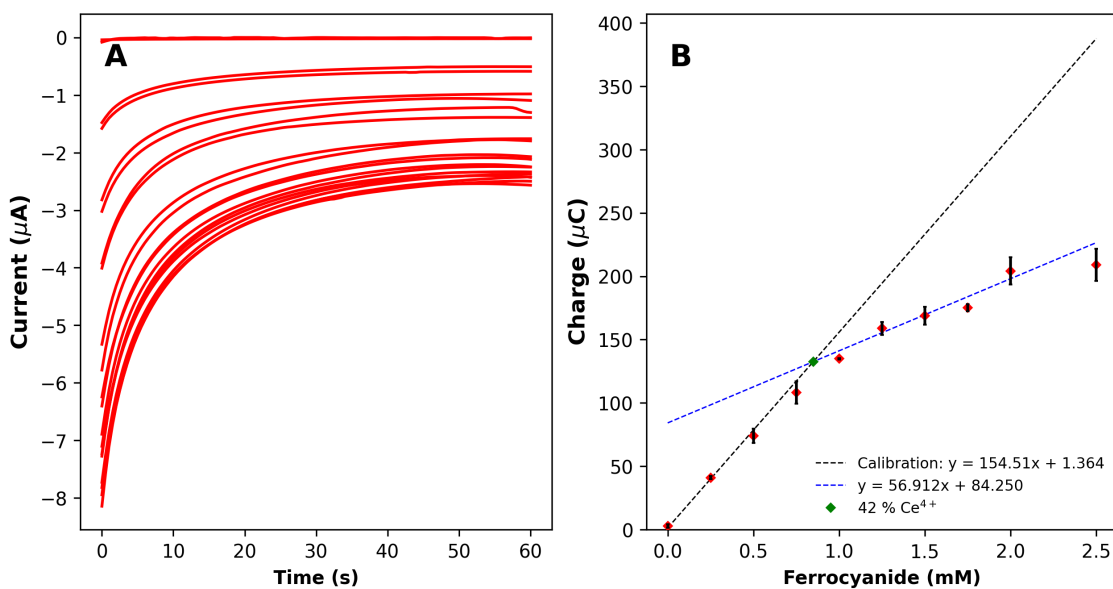


Figure E.1: Raw chronoamperometry data of in-home 3 nm cerias (**A**) and the treated data by means of their integral (charge) (**B**), resembling the same compositional graphs as for kinetic studies.  $n = 2$  with an incubation of 1 h.

# Bibliography

- [1] Wing Cheung Mak, Valerio Beni, and Anthony P.F. Turner. Lateral-flow technology: From visual to instrumental. *TrAC Trends in Analytical Chemistry*, 79:297–305, 2016. ISSN 0165-9936. doi: <https://doi.org/10.1016/j.trac.2015.10.017>. URL <https://www.sciencedirect.com/science/article/pii/S0165993615301084>. Past , Present and Future challenges of Biosensors and Bioanalytical tools in Analytical Chemistry: a tribute to Prof Marco Mascini.
- [2] Donald G. Klepser, Nicklas S. Klepser, Jennifer L. Adams, Alex J. Adams, and Michael E. Klepser. The impact of the covid-19 pandemic on addressing common barriers to pharmacy-based point-of-care testing. *Expert Review of Molecular Diagnostics*, 21(8):751–755, 2021. doi: 10.1080/14737159.2021.1944105.
- [3] Jobie Budd, Benjamin S. Miller, Nicole E. Weckman, Dounia Cherkaoui, Da Huang, and Alyssa Thomas. Lateral flow test engineering and lessons learned from covid-19. *Nature Reviews Bioengineering*, 1:13–31, 2023. doi: <https://doi.org/10.1038/s44222-022-00007-3>.
- [4] B. O’Farrell. Lateral flow immunoassay systems: Evolution from the current state of the art to the next generation of highly sensitive, quantitative rapid assays. *The Immunoassay Handbook*, pages 89–107, 12 2013. doi: 10.1016/B978-0-08-097037-0.00007-5.
- [5] Ralph Müller and Doris Clegg. Automatic paper chromatography. *Annals of the New York Academy of Sciences*, 53:1108 – 1118, 12 2006. doi: 10.1111/j.1749-6632.1951.tb48886.x.
- [6] Eva Engvall and Peter Perlmann. Enzyme-linked immunosorbent assay (elisa) quantitative assay of immunoglobulin g. *Immunochemistry*, 8(9):871–874, 1971. ISSN 0019-2791. doi: [https://doi.org/10.1016/0019-2791\(71\)90454-X](https://doi.org/10.1016/0019-2791(71)90454-X). URL <https://www.sciencedirect.com/science/article/pii/001927917190454X>.
- [7] B.K. Van Weemen and A.H.W.M. Schuurs. Immunoassay using antigen—enzyme conjugates. *FEBS Letters*, 15(3):232–236, 1971. ISSN 0014-5793. doi: [https://doi.org/10.1016/0014-5793\(71\)80319-8](https://doi.org/10.1016/0014-5793(71)80319-8). URL <https://www.sciencedirect.com/science/article/pii/0014579371803198>.
- [8] Diagnostic testing for sars-cov-2, 2020. URL <https://www.who.int/publications/i/item/diagnostic-testing-for-sars-cov-2>.
- [9] Use of sars-cov-2 antigen-detection rapid diagnostic tests for covid-19 self-testing, 2022. URL <https://www.who.int/publications/i/item/WHO-2019-nCoV-Ag-RDTs-Self-testing-2022.1>.

- [10] The act-accelerator: Two years of impact, 2022. URL <https://www.who.int/publications/m/item/the-act-accelerator--two-years-of-impact>.
- [11] Antigen testing guidelines, 2023. URL <https://www.cdc.gov/coronavirus/2019-ncov/lab/resources/antigen-tests-guidelines.html>.
- [12] Kevin Land, Debrah I Boeras, Xiang-Sheng Chen, Andrew Ramsay, and Rosanna W Peeling. Reassured diagnostics to inform disease control strategies, strengthen health systems and improve patient outcomes. 4(1):46–54, Jan 2019. doi: <https://doi.org/10.1038/s41564-018-0295-3>. URL <https://www.nature.com/articles/s41564-018-0295-3#citeas>.
- [13] Evgeni Eltzov, Sarah Guttel, Adarina Low Yuen Kei, Prima Dewi Sinawang, Rodica E. Ionescu, and Robert S. Marks. Lateral flow immunoassays – from paper strip to smartphone technology. *Electroanalysis*, 27(9):2116–2130, 2015. doi: <https://doi.org/10.1002/elan.201500237>. URL <https://analyticalsciencejournals.onlinelibrary.wiley.com/doi/abs/10.1002/elan.201500237>.
- [14] Andrea J. MacNeill, Harriet Hopf, Aman Khanuja, Saed Alizamir, Melissa Bilec, Matthew J. Eckelman, Lyndon Hernandez, Forbes McGain, Kari Simonsen, Cassandra Thiel, Steven Young, Robert Lagasse, and Jodi D. Sherman. Transforming the medical device industry: Road map to a circular economy. *Health Affairs*, 39(12):2088–2097, 2020. doi: [10.1377/hlthaff.2020.01118](https://doi.org/10.1377/hlthaff.2020.01118).
- [15] Dmitry Galyamin, Susana Liébana, Juan Cruz Esquivel, and Neus Sabaté. Immuno-battery: A single use self-powered immunosensor for reassured diagnostics. 220:114868–114868, Jan 2023. doi: <https://doi.org/10.1016/j.bios.2022.114868>. URL <https://pubmed.ncbi.nlm.nih.gov/36356482/>.
- [16] Farnoosh Attar, Mahsa Ghofrani Shahpar, Behnam Rasti, Majid Sharifi, Ali Akbar Saboury, Seyed Mahdi Rezayat, and Mojtaba Falahati. Nanozymes with intrinsic peroxidase-like activities. *Journal of Molecular Liquids*, 278:130–144, 2019. ISSN 0167-7322. doi: <https://doi.org/10.1016/j.molliq.2018.12.011>. URL <https://www.sciencedirect.com/science/article/pii/S0167732218341965>.
- [17] Atul Dhall and William Self. Cerium oxide nanoparticles: A brief review of their synthesis methods and biomedical applications. *Antioxidants*, 7(8), 2018. ISSN 2076-3921. doi: [10.3390/antiox7080097](https://doi.org/10.3390/antiox7080097). URL <https://www.mdpi.com/2076-3921/7/8/97>.
- [18] Dmitry Galyamin, Lena M. Ernst, Aina Fitó-Parera, Guillem Mira-Vidal, Neus G. Bastús, Neus Sabaté, and Victor Puntes. Nanoceria dissolution at acidic ph by breaking off the catalytic loop. *Nanoscale*, 14:14223–14230, 2022. doi: [10.1039/D2NR03586C](https://doi.org/10.1039/D2NR03586C). URL <http://dx.doi.org/10.1039/D2NR03586C>.
- [19] P. Dutta, S. Pal, M. S. Seehra, Y. Shi, E. M. Eyring, and R. D. Ernst. Concentration of ce<sup>3+</sup> and oxygen vacancies in cerium oxide nanoparticles. *Chemistry of Materials*, 18(21):5144–5146, Oct 2006. ISSN 0897-4756. doi: [10.1021/cm061580n](https://doi.org/10.1021/cm061580n). URL <https://doi.org/10.1021/cm061580n>.
- [20] R.K. Franklin, S.M. Martin, T.D. Strong, and R.B. Brown. Chemical and biological systems: Chemical sensing systems for liquids. In *Reference Module in Materials Science and Materials Engineering*. Elsevier, 2016. ISBN 978-0-12-803581-8. doi: <https://doi.org/10.1016>

- B978-0-12-803581-8.00549-X. URL <https://www.sciencedirect.com/science/article/pii/B978012803581800549X>.
- [21] Jan Krejci, Zuzana Sajdlova, Vilem Nedela, Eva Flodrova, Romana Sejnohova, Hana Vranova, and Robert Plicka. Effective surface area of electrochemical sensors. *Journal of The Electrochemical Society*, 161(6):B147, may 2014. doi: 10.1149/2.091406jes. URL <https://dx.doi.org/10.1149/2.091406jes>.
  - [22] Adam E Cohen and Roderick R Kunz. Large-area interdigitated array microelectrodes for electrochemical sensing. *Sensors and Actuators B: Chemical*, 62(1):23–29, 2000. ISSN 0925-4005. doi: [https://doi.org/10.1016/S0925-4005\(99\)00372-X](https://doi.org/10.1016/S0925-4005(99)00372-X). URL <https://www.sciencedirect.com/science/article/pii/S092540059900372X>.
  - [23] Ekaterina V Tsimpis and Vladislav V Kharton. Electrode materials and reaction mechanisms in solid oxide fuel cells: a brief review. 12(11):1367–1391, Jul 2008. doi: <https://doi.org/10.1007/s10008-008-0611-6>. URL <https://link.springer.com/article/10.1007/s10008-008-0611-6#citeas>.
  - [24] Lianqing Liu, Yuan-Ting Li, Dawei Li, and Yi-Tao Long. Recent developments and applications of screen-printed electrodes in environmental assays—a review. 734:31–44, Jul 2012. doi: <https://doi.org/10.1016/j.aca.2012.05.018>. URL <https://pubmed.ncbi.nlm.nih.gov/22704470/>.
  - [25] Dennis H. Evans and Michael J. Kelly. Theory for double potential step chronoamperometry, chronocoulometry, and chronoabsorptometry with a quasi-reversible electrode reaction, 1982. URL <https://pubs.acs.org/doi/10.1021/ac00248a016>.
  - [26] C.G.J. Koopal, B. Eijsma, and R.J.M. Nolte. Chronoamperometric detection of glucose by a third generation biosensor constructed from conducting microtubules of polypyrrole. *Synthetic Metals*, 57(1):3689–3695, 1993. ISSN 0379-6779. doi: [https://doi.org/10.1016/0379-6779\(93\)90498-L](https://doi.org/10.1016/0379-6779(93)90498-L). URL <https://www.sciencedirect.com/science/article/pii/037967799390498L>. Proceedings of the International Conference on Science and Technology of Synthetic Metals.
  - [27] Javier Moral-Vico, Jaume Barallat, Llibertat Abad, Rosa Olivé-Monllau, Francesc Xavier Muñoz-Pascual, Amparo Galán Ortega, F. Javier del Campo, and Eva Baldrich. Dual chronoamperometric detection of enzymatic biomarkers using magnetic beads and a low-cost flow cell. *Biosensors and Bioelectronics*, 69:328–336, 2015. ISSN 0956-5663. doi: <https://doi.org/10.1016/j.bios.2015.02.042>. URL <https://www.sciencedirect.com/science/article/pii/S0956566315001554>.
  - [28] Kevin C. Honeychurch. Printed thick-film biosensors, 2012. URL <https://uwe-repository.worktribe.com/output/944748>.
  - [29] Max Planck. *The theory of heat radiation*, volume 162 (5). 1914. URL <https://archive.org/details/theoryofheatradi00planrich>.
  - [30] Pierre Bouguer and Lionel Simonot. *Essai d'optique sur la gradation de la lumière*. October 2021. URL <https://hal.science/hal-03980585>.
  - [31] J. H. Lambert. *Photometria sive de mensura et gradibus luminis, colorum et umbrae*. 1760. URL [https://archive.org/details/T00E039861\\_T00324\\_PNI-2733\\_000000](https://archive.org/details/T00E039861_T00324_PNI-2733_000000).

- [32] Beer. *Bestimmung der Absorption des rothen Lichts in farbigen Flüssigkeiten*, volume 162 (5). 1852. doi: 10.1002/andp.18521620505. URL [https://archive.org/details/T00E039861\\_T00324\\_PNI-2733\\_000000](https://archive.org/details/T00E039861_T00324_PNI-2733_000000).
- [33] Ignacio Salvo Ibáñez. Control and synthesis of cerium oxide nanoparticles for medical applications. *Tesisenred.net*, 2019. doi: <https://doi.org/9788449085857>. URL <https://www.tesisenred.net/handle/10803/666824#page=1>.
- [34] Beat Müller, Mirjam Christ-Crain, Eric S. Nylen, Richard Snider, and Kenneth L. Becker. Limits to the Use of the Procalcitonin Level as a Diagnostic Marker. *Clinical Infectious Diseases*, 39(12):1867–1868, 12 2004. ISSN 1058-4838. doi: 10.1086/426148. URL <https://doi.org/10.1086/426148>.
- [35] Boris N. Khlebtsov, Roman S. Tumskiy, Andrey M. Burov, Timofey E. Pylaev, and Nikolai G. Khlebtsov. Quantifying the numbers of gold nanoparticles in the test zone of lateral flow immunoassay strips. *ACS Applied Nano Materials*, 2(8):5020–5028, 2019. doi: 10.1021/acsanm.9b00956. URL <https://doi.org/10.1021/acsanm.9b00956>.
- [36] David A Armbruster and Terry Pry. Limit of blank, limit of detection and limit of quantitation. *The Clinical biochemist. Reviews*, 29 Suppl 1(Suppl 1):S49–52, 2008. URL <https://www.ncbi.nlm.nih.gov/pmc/articles/PMC2556583/#:~:text=LoB%20is%20the%20highest%20apparent,containing%20no%20analyte%20are%20tested.&text=LoD%20is%20the%20lowest%20analyte,at%20which%20detection%20is%20feasible>.
- [37] N. V. Skorodumova, S. I. Simak, B. I. Lundqvist, I. A. Abrikosov, and B. Johansson. Quantum origin of the oxygen storage capability of ceria. *Phys. Rev. Lett.*, 89:166601, Sep 2002. doi: 10.1103/PhysRevLett.89.166601. URL <https://link.aps.org/doi/10.1103/PhysRevLett.89.166601>.
- [38] Christoph Loschen, Annappaola Migani, Stefan T Bromley, Francesc Illas, and Konstantin M Neyman. Density functional studies of model cerium oxide nanoparticles. 10(37):5730–5730, Jan 2008. doi: <https://doi.org/10.1039/b805904g>. URL <https://pubs.rsc.org/en/content/articlelanding/2008/cp/b805904g/unauth>.
- [39] Mohammed Baalousha, Yon Ju-Nam, Paula A Cole, Birgit Gaiser, Teresa F Fernandes, Joseph A Hriljac, Mark A Jepson, Vicki Stone, Charles R Tyler, and Jamie R Lead. Characterization of cerium oxide nanoparticles-part 1: Size measurements. 31(5):983–993, Mar 2012. doi: <https://doi.org/10.1002/etc.1785>. URL <https://pubmed.ncbi.nlm.nih.gov/22368045/>.
- [40] Yun Kong, Nam Ho Heo, Ji-Won Kang, Jin Yong Lee, Hae Jin Kim, and Moon S Kim. Nanoceria-based lateral flow immunoassay for hydrogen peroxide-free colorimetric biosensing for c-reactive protein. 414(10):3257–3265, Jan 2022. doi: <https://doi.org/10.1007/s00216-022-03877-z>. URL <https://link.springer.com/article/10.1007/s00216-022-03877-z>.
- [41] Xuemei Li, Li Sun, Anqing Ge, and Yingshu Guo. Enhanced chemiluminescence detection of thrombin based on cerium oxide nanoparticles. 47(3):947–949, Jan 2011. doi: <https://doi.org/10.1039/c0cc03750h>. URL <https://pubs.rsc.org/en/content/articlelanding/2011/cc/c0cc03750h/unauth>.

- [42] Yeni Wahyuni Hartati, Leonard Kristofel Letelay, Shabarni Gaffar, Santhy Wyantuti, and Husein H. Bahti. Cerium oxide-monoclonal antibody bioconjugate for electrochemical immunosensing of her2 as a breast cancer biomarker. *Sensing and Bio-Sensing Research*, 27:100316, 2020. ISSN 2214-1804. doi: <https://doi.org/10.1016/j.sbsr.2019.100316>. URL <https://www.sciencedirect.com/science/article/pii/S2214180419301357>.
- [43] Anton Popov, Alexander B Shcherbakov, Nadezhda Zholobak, and Vladimir K Ivanov. Cerium dioxide nanoparticles as third-generation enzymes (nanozymes), Dec 2017. URL [https://www.researchgate.net/publication/322141454\\_Cerium\\_dioxide\\_nanoparticles\\_as\\_third-generation\\_enzymes\\_nanozymes](https://www.researchgate.net/publication/322141454_Cerium_dioxide_nanoparticles_as_third-generation_enzymes_nanozymes).
- [44] Baskaran Stephen Inbaraj and Bing-Huei Chen. An overview on recent in vivo biological application of cerium oxide nanoparticles. *Asian Journal of Pharmaceutical Sciences*, 15 (5):558–575, 2020. ISSN 1818-0876. doi: <https://doi.org/10.1016/j.ajps.2019.10.005>. URL <https://www.sciencedirect.com/science/article/pii/S1818087619305033>.
- [45] Muhammad Usama Marghoob, Aasma Noureen, Ali Raza, Waheed S. Khan, Mehwish Iftikhar, and Farooq Sher. Synthesis and toxicity assessment of environment friendly high yield ceria nanoparticles for biosafety. *Journal of Environmental Chemical Engineering*, 10(1):107029, 2022. ISSN 2213-3437. doi: <https://doi.org/10.1016/j.jece.2021.107029>. URL <https://www.sciencedirect.com/science/article/pii/S2213343721020066>.
- [46] Peng Zhang, Yuhui Ma, Zhiyong Zhang, Xiao He, Yuanyuan Li, Jing Zhang, Lirong Zheng, and Yuliang Zhao. Species-specific toxicity of ceria nanoparticles to lactuca plants. *Nanotoxicology*, 9(1):1–8, 2015. doi: 10.3109/17435390.2013.855829. URL <https://doi.org/10.3109/17435390.2013.855829>. PMID: 24256192.
- [47] Ninett Gäbler, Jennifer Hartley, and Gero Frisch. Voltammetric and spectroscopic study of ferrocene and hexacyanoferrate and the suitability of their redox couples as internal standards in ionic liquids. *Phys. Chem. Chem. Phys.*, 19, 09 2017. doi: 10.1039/C7CP05483A.